Green and Smart Mining Engineering 1 (2024) 104–117

Contents lists available at ScienceDirect

Green and Smart Mining Engineering

journal homepage: www.keaipublishing.com/en/journals/gsme

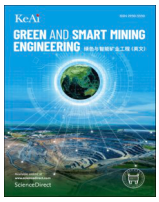

Effect of blast furnace slag substitution for cement in carbon-reduced and low-cost solidified/stabilized cementitious materials

Siqi Zhang[a,*,1], Tong Zhao[a,1], Keqing Li[a], Wen Ni[a,*], Huifen Yang[a], Zeping Wu[a], Jia Li[a], Yue Li[a], Bo Zhang[a], Jiajia Wang[a], Runsheng Xu[b], Xiaoming Liu[b], Pingfeng Fu[a], Weihua Cui[c], Jun Yao[c]

[a] School of Civil and Resource Engineering, University of Science and Technology Beijing, Beijing 100083, China
[b] School of Metallurgical and Ecological Engineering, University of Science and Technology Beijing, Beijing 100083, China
[c] School of Water Resources and Environment, China University of Geosciences (Beijing), Beijing 100083, China

ARTICLE INFO

Keywords:
Low-carbon cementitious materials
Multisolid waste synergy
CO_2 emissions
Fly ash
Blast furnace slag
Desulfurization gypsum

ABSTRACT

The development of low-carbon cementitious materials involves the selection of the appropriate raw materials and the transformation of the hydration mechanism. In this study, low-carbon and low-cost cementitious materials were prepared using municipal solid waste incineration fly ash (MSWI FA), blast furnace slag (BFS), and desulfurization gypsum (DFG) as raw materials to reduce clinker usage. Results showed that the compressive strength of K5 (mass ratio of BFS: DFG: MSWI FA = 7:1:2) after 360 d of curing was 41.49 MPa, with a low leaching concentration of heavy metal residues that meet groundwater Class II standards, a dioxin content of only 25 ngTEG/kg, and a stable pH value ranging between 11 and 11.5. Microscopic analysis revealed a continuous decrease in the Ca/Si atomic ratios of K4 (mass ratio of BFS: DFG: MSWI FA: P·I 42.5 = 42:10:20:28) and K5, i.e., 1.18–1.54 and 1.04–1.23, respectively, with the increase in the hydration age. The highest Al/Si atomic ratio of K5, i.e., 0.26–0.31, was observed with the strongest conversion trend of calcium–silicate–hydrate gel into calcium–aluminum–silicate–hydrate gel, and the network structure of sodium–(calcium)–aluminum–silicate–-hydrate gel zeolite-like phase was generated. The water-to-binder (WTB) mass ratio of 0.35 was determined to be more suitable for the K4 and K5 systems and resulted in a 56.83% and 90.82% reduction in half-life t_∂ compared with the WTB ratio of 0.5, respectively. Notably, the value of the reaction velocity constant K in the induction period was 10 times that of K1, and the autocatalytic reaction controlled the value of N to < 1. The X-ray absorption near-edge structure indicated that Zn solidification produced Zn_2SiO_4 with a small solubility product. The production of 1 t of K5 emitted only 10.83 kg/t of CO_2, which was 40 times less than that of K1. Overall, K5 provides the highest economic benefit at 40.08 USD/t, and the clinker-free cementitious system with multisolid waste synergy has significant advantages in terms of solidifying harmful substances, reducing carbon emissions, and lowering costs.

1. Introduction

China's domestic waste incineration industry has grown rapidly, with the mechanical grate furnace process being used in approximately 90% of incineration projects. However, the resulting municipal solid waste incineration fly ash (MSWI FA) is classified as HW18 on China's hazardous waste list because of the high levels of pollutants, such as chlorine salts, dioxins, and easily soluble heavy metals [1]. The disposal costs of MSWI FA have reached 300–600 USD/t in Tier 1 cities. By 2025, the annual production of fly ash is expected to reach 10 million t, which is approximately 10% of China's total hazardous waste [2].

Currently, the most common methods for MSWI FA disposal are cement solidification/stabilization (S/S) and safe landfilling [3]. The cement solidification process is a mature and cost-effective technology in which MSWI FA is encapsulated by calcium–silicate–hydrate (C–S–H) gel and other hydration products [4,5]. However, the composition of MSWI FA is highly variable, and the presence of soluble chloride salts can affect the long-term stability of dioxins and heavy metals in the

Peer review under the responsibility of Editorial Board of Green and Smart Mining Engineering.
* Corresponding authors.
E-mail addresses: zsq2017@ustb.edu.cn (S. Zhang), niwen@ces.ustb.edu.cn (W. Ni).
[1] These authors contributed equally.

https://doi.org/10.1016/j.gsme.2024.01.001
Received 13 November 2023; Received in revised form 23 December 2023; Accepted 29 January 2024
Available online 22 March 2024

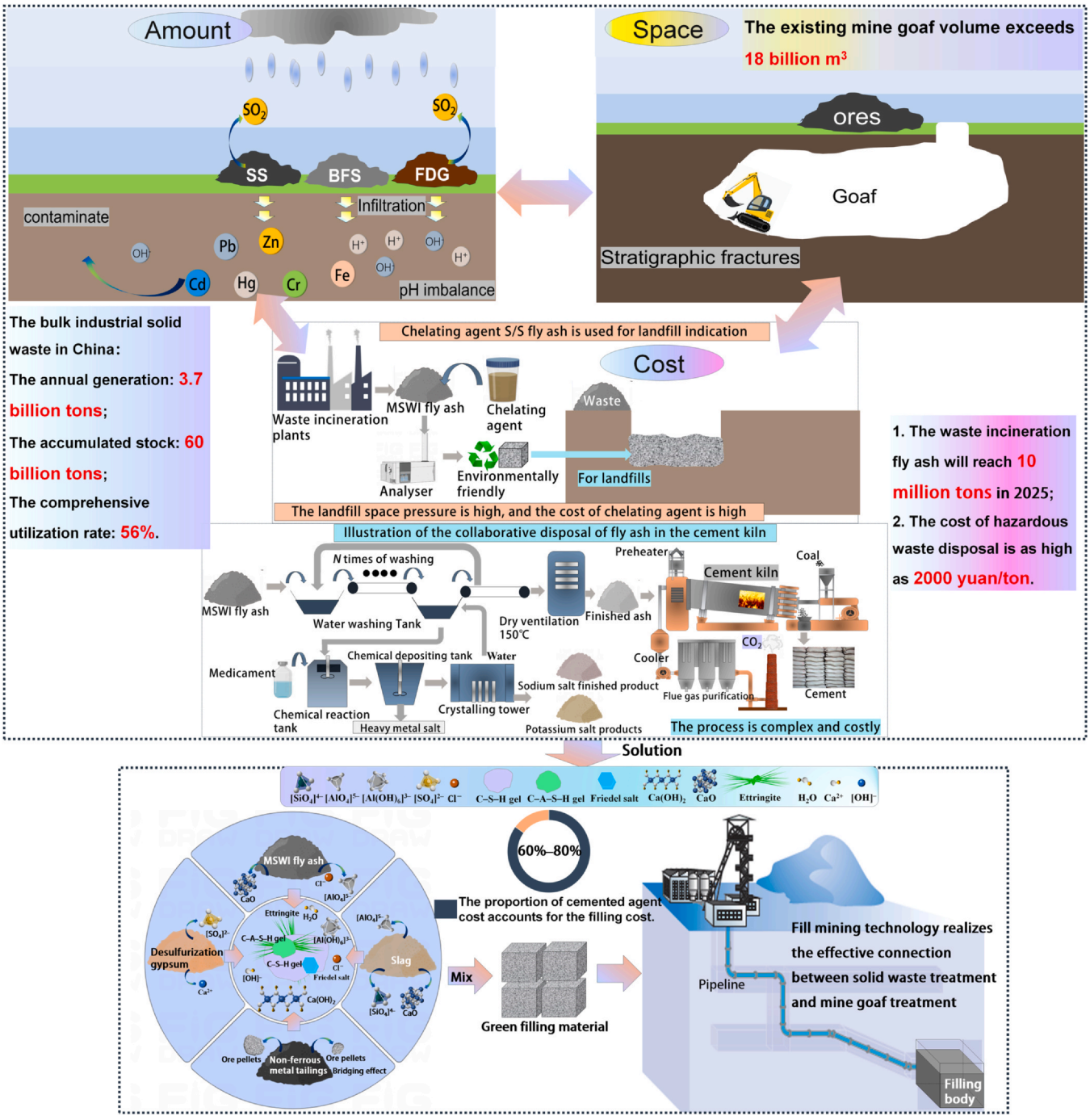

Fig. 1. Three-factor diagram of quantity–space–cost.

solidified body [6–10]. Furthermore, the harmful elements in MSWI FA can have complex effects on the cementitious system, affecting the compressive strength and coagulation period. Studies have shown [11–14] that heavy metals, such as Pb, Cu, As, Zn, Cr, and Cd, can hinder hydration heat release, delay the setting time, and reduce compressive strength. Cement-based systems also exhibit low compatibility with oxygen anions and amphoteric metal ions, which can inhibit cement hydration.

China has achieved carbon neutrality, which has resulted in increasing cement prices and changes in the cement industry. Studies [15–19] have shown that solid-waste-based cementitious materials, such as blast furnace slag (BFS) and coal fly ash (CFA), can replace cement with improved hydration activity and resistance to water-soluble chlorine and acid corrosion. The combination of MSWI FA and BFS improves gelling activity and solidifies dioxins and heavy metals. Solid-waste-based clinker-free filling materials have been developed using BFS and steel slag powder, with leaching concentrations of dioxins and heavy metal ions that meet drinking water standards. Generally, the BFS glass structure disintegrates into unstable structural units, induces the reaction, and forms a dispersion–condensation thixotropic structure and an ordered precursor, following which the hydrates generate a new polycondensation crystal structure. Under alkali excitation conditions, traditional cement hydration products primarily generate high Ca/Si atomic ratios of tobermorite–jennite-structured C–S–H gels with an average Ca/Si atomic ratio of > 1.6, whereas glassy solid waste typically generates low C–S–H gels with an average Ca/Si atomic ratio of < 1.2. The conversion of C–S–H and calcium–aluminum–silicate–hydrate (C–A–S–H) gels is influenced by the Ca/Si atomic

ratio, which promotes the formation of longer chains and tightly crystalline structures and ensures the compactness of the solidified body [20,21].

Scholars have investigated the S/S mechanism of heavy metals in MSWI FA using various microscopic analysis methods. For instance, Zn is immobilized by the formation of stable silicates and amorphous Zn $(OH)_2$ hydroxide complex salts, which are adsorbed by C–S–H gels, ettringites, and calcium chloroaluminate hydrates [22]. Pb is encapsulated in the C–S–H gel to form Pb–O–Si chemical bonds and stabilized as $Pb_4(OH)_4^{4+}$ and $PbSiO_3$ stable silicates through adsorption by silica, silicon chain [23], and C_3S. Cr(VI) can be reduced to Cr(III) and undergo ion exchange with Al(III) in alumina, adsorbed on Friedel's salt, or replaced SO_4^{2-} in ettringite to form a solid solution [24–26]. Cr also forms a $CaCrO_4{\cdot}2H_2O$ crystalline phase and adsorbs on the porous surface of the C–S–H gel. Cu, Cd, and Ni participate in hydration reactions and precipitate hydroxides, such as $Cu(OH)_2$, $CaCd(OH)_4$, and $Ni(OH)_2$, and replace Ca^{2+} for charge compensation by combining with the deprotonated silanol group in C–S–H/C–A–S–H gels [9,10].

Researchers [3,27] have investigated the S/S mechanism of heavy metals in MSWI FA using new magnesium sulfate and phosphate cement. The S/S mechanism of heavy metals was investigated using X-ray diffraction (XRD) and extended X-ray absorption fine structure analyses, which revealed that phosphate precipitation in the MSWI FA–-phosphate cement binder is crucial for solidifying Zn and Cu, whereas the MSWI FA–sulfate cement binder exhibits high fixation efficiency (99.8%) for both Pb and As [28,29]. MSWI FA shows volcanic ash activity, and the combined assistance of soluble cations and anions excites the amorphous phase dissolution of glassy solid waste to yield various types of C–(A)–S–H gel solid solutions along with low-solubility complex salts. Desulfurization gypsum (DFG) can be used as a sulfate initiator in synergy with BFS and steel slag to generate ettringite minerals. In the simulated application scenarios, the leaching concentration of harmful substances was less than the drinking water standard (Chinese National Standard GB 5749–2006). However, the in-depth S/S mechanism of heavy metals, the amorphous phase transition process, and the factors affecting the recombination excitation rate require further investigation. This research can help address issues related to the disposal and recycling of MSWI FA, mine cementation, filling mining, and high cement costs (as depicted in Fig. 1).

Therefore, this study comprehensively investigates the amorphous phase structure–crystal phase transition process during the hydration process of BFS–MSWI FA–DFG by employing several qualitative and semiquantitative microscopic analyses of hydration heat and fitting kinetic parameters, in addition to quantitative speciation analysis of heavy metals with X-ray absorption fine structure (XAFS) analysis for fitting the atomic bond length. Based on the calculated solubility and degree of polymerization of a vitreous body, combined with the thermal/kinetic parameters, the variations in the hydration products and the evolution of the microstructure of solidified bodies were revealed, which elucidated the S/S form, endowed status, and migration transformation of harmful substances. This study aims to establish a theoretical foundation for the resource utilization of clinker-free cement or low-clinker cement-containing MSWI-FA-based low-carbon and ultralow-cost cementitious materials, as well as the S/S of harmful substances.

2. Experimental

2.1. Materials

MSWI FA used in this study originated from a grate furnace waste incineration power plant situated in Beijing, China. Table S1 shows that the predominant mineral constituents of MSWI FA were identified as CaO and Cl, constituting 34.96% and 20.12% of the mass fractions composition, respectively. Additionally, the mass fraction contents of SO_3 and Na_2O are 7.97% and 6.63% respectively. Fig. S1 shows the phase composition analysis of the raw material, revealing the high crystallinity of the primary peaks in MSWI FA, which are predominantly composed of NaCl, KCl, and $CaSO_4$ phases.

Table S2 lists the particle sizes of MSWI FA, indicating a fine and uniform distribution without noticeable graininess. The D_{10}, D_{50}, and D_{90} values for cumulative particle size distribution at the mass fractions of 10%, 50%, and 90% are $<$ 1.83, 4.01, and 5.87 μm respectively. To assess the leachate concentration of harmful target elements, the untreated MSWI FA ash underwent a horizontal oscillation leaching test, following the Chinese National Environmental Protection Standard HJ 557–2010, with measurements conducted using inductively coupled plasma mass spectrometry (ICP-MS) on a Thermo ICAP 7200 DUO instrument. Following the Chinese National Standard for Groundwater Quality GB/T 14848–2017, the concentrations of five heavy metals (i.e., Pb, Zn, Cd, Cr, and Hg) in MSWI FA were evaluated. Tables S3 and S4 present the varying degrees of excess, with Pb and Cr exhibiting significant deviations beyond the standard limits.

Following the Chinese National Environmental Protection Standard HJ 77.3–2008, the toxic equivalent concentration (ng-TEQ/kg) of dioxins in MSWI FA was assessed using the polychlorinated dibenzo-p-dioxins (PCDD) and polychlorinated dibenzofurans (PCDF) isotope dilution high resolution gas chromatography–high resolution mass spectrometry (HRGC/HRMS) hazardous waste determination method (Table S5). The results showed that the concentration of 556 ng-TEQ/kg significantly exceeded the standard limit of 50 ng-TEQ/kg specified in the technical specification for controlling MSWI FA pollution in domestic waste incineration (Chinese National Environmental Protection Standard HJ 1134–2020). This finding highlights the substantially higher level of harm associated with the dioxin content in the MSWI FA sample. The physical and chemical properties of BFS, DFG, and P·I 42.5 Portland cement are presented in Supplementary Material.

2.2. Preparation of the test samples

BFS was oven-dried at 100 °C for 24 h to achieve a moisture mass content of 5%. Similarly, DFG was oven-dried at 50 °C for 72 h to achieve the desired moisture content. In this study, the formulation variables considered the BFS content as a weight percentage of the cementitious material, gradually replacing the cement at levels of 0%, 14%, 28%, 42%, and 70%. Previous research [28,29] provided insights into the optimal proportions of other constituents, with an optimal MSWI FA mass content of 20% and a DFG mass content of 10%. Table S6 lists the different proportions of cementitious materials with a water-to-binder (WTB) mass ratio of 0.35. The sample preparation method used in this study is consistent with the approach described in our previous investigation [28]. After specific time intervals of 3, 7, 28, 90, 180, and 360 d, the samples were subjected to compressive strength tests in triplicate. Following the compressive strength tests, the samples were dried to halt the hydration reaction. Subsequently, the samples were prepared for the leaching characteristic tests and ground to a particle size exceeding of 95% mass content by passing through a 200-mesh sieve to ensure consistency for microscopic examinations and analyses.

2.3. Mechanical properties and leaching tests of the backfill materials

The compressive strengths of cementitious materials were determined following the test method outlined in the Chinese National Standard GB/T 17671–1999, which is based on the ISO method. These results were determined to be consistent with the findings reported by Li *et al.* [28], who employed a similar test method.

To simulate the leaching behavior of the solidified cementitious material after S/S treatment, leaching toxicity tests were conducted using the horizontal vibration method specified in the Chinese National Environmental Protection Standard HJ/T 557–2010. The S/S samples were crushed and sieved to particle sizes smaller than 3 mm.

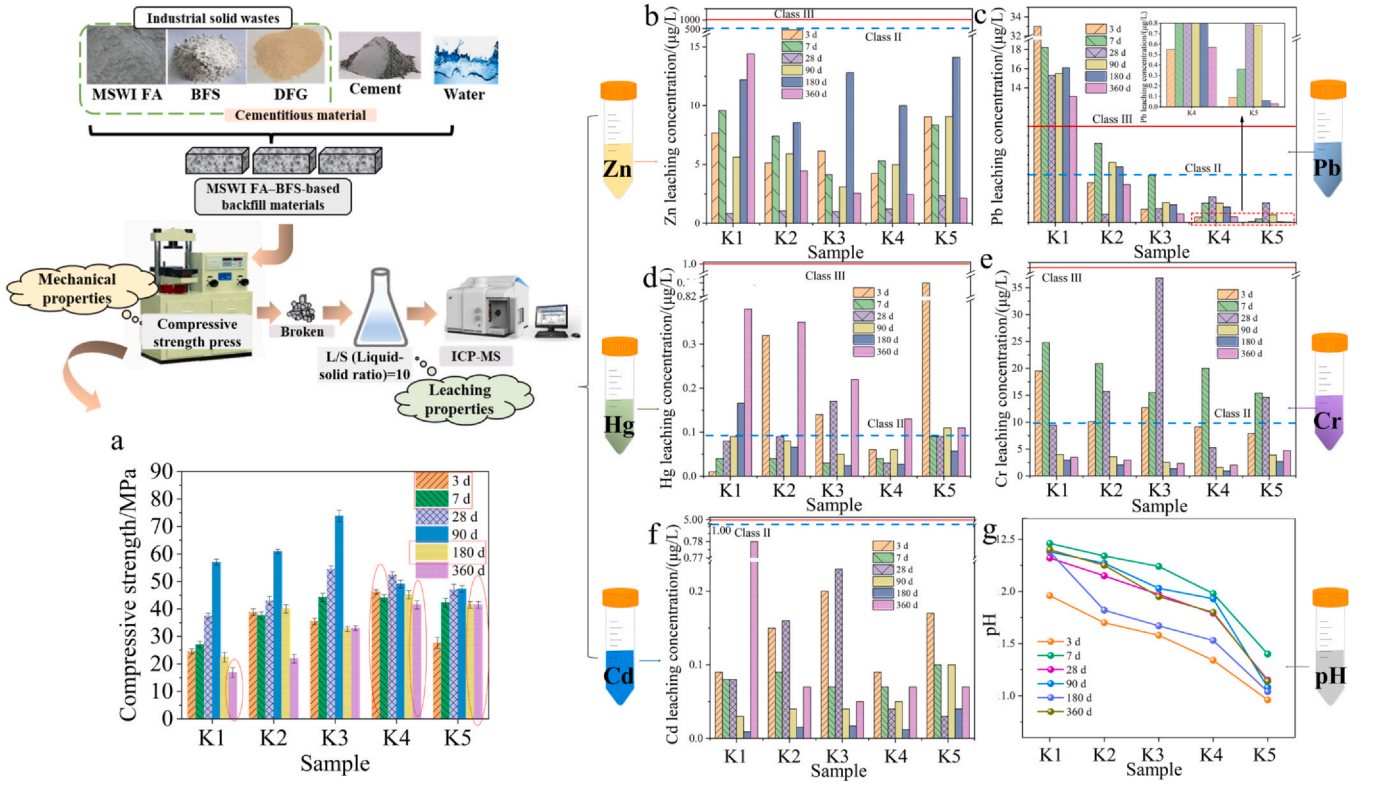

Fig. 2. Preparation and performance test methods of the K1–K5 test blocks for 3, 7, 28, 90, 180, and 360 d: (a) compressive strength, (b) Zn leaching concentration, (c) Pb leaching concentration, (d) Hg leaching concentration, (e) Cr leaching concentration, (f) Cd leaching concentration, and (g) leaching solution pH variation after solidifying for 3, 7, 28, 90, 180, and 360 d.

Subsequently, deionized water was added to 50 g of the sieved material at a liquid-to-solid ratio of 10 L/kg. The mixture was horizontally shaken at a frequency of 110 ± 10 times/min for 8 h at room temperature (20 °C) and left to settle for 16 h. The resulting leachates were filtered using 0.45-μm polypropylene membrane filters, preserved with HNO_3, and stored at 4 °C. The concentrations of Pb, Zn, Cr, Hg, and Cd in the leachates were determined using ICP-MS. The concentration of dioxins in the cementitious materials was determined following the specified standards and methods for dioxin analysis in MSWI FA.

2.4. Microanalysis of the paste

Microanalysis of the cementitious paste was conducted using various techniques. Heavy metal speciation, XRD, X-ray photoelectron spectroscopy (XPS), and XAFS were used for the quantitative and qualitative analyses of heavy metals, such as Pb, Zn, Cr, Cd, and Hg. The hydration structures of the paste were qualitatively analyzed using XRD, Fourier transform infrared spectroscopy (FTIR), thermogravimetric analysis–differential scanning calorimetry (TG–DSC), scanning electron microscopy–energy-dispersive spectroscopy (SEM–EDS), XPS, and isothermal conduction calorimetry. The analytical steps for heavy metal speciation are detailed in Table S7. The specific testing instruments and steps are presented in Supplementary Material.

Isothermal conduction calorimetry was conducted to analyze the hydration heat release of the K1, K4, and K5 pastes. The isothermal conduction calorimeter was connected to an exothermic meter and a nitrogen cylinder, and the experiment was conducted following the Chinese National Standard GB/T 12959–2008. To investigate the kinetic behavior and activities of cement-based materials and BFS during the exothermic hydration reaction. The process of fitting the formula is described in detail in Supplementary Material.

In this study, we conducted XAFS experiments at the Beijing Synchrotron Radiation Facility, Institute of High Energy Physics, Chinese Academy of Sciences. Given the low zinc (Zn) content in the solution standard, we employed the fluorescence mode. The XAFS spectra of the Zn LIII absorption edge were obtained for the K1, K4, and K5 samples, corresponding to curing periods of 7, 90, and 360 d, respectively. The energy scanning range spanned from 9.460 to 10.460 keV. Before the absorption edge, energy steps of 4 eV were used, followed by 1 eV near the edge and 2 and 4 eV after the edge, for both the fluorescence and transfer modes. The acquired spectral data were processed and analyzed using Athena software. The standard data processing steps for the synchrotron radiation data, including normalization, *E–k* transformation, Fourier transformation, and shell fitting, were conducted. The *E–k* transformation refers to the conversion of XAFS data in energy space, c(*E*), to wavevector space, c(*k*). To further elucidate the micromolecular structure of the Zn compounds in the cured samples, we used the crystallographic information file (CIF) file of the acquired compounds along with real space Green's function code (FEFF software) theory calculations and nonlinear least squares fitting. We determined the coordination number of Zn ions, bond length, energy correction ΔE_0, and *R* factor to assess the quality of the fitting procedure. The experimental parameters and fitting steps are presented in the Supplementary Material.

2.5. Life cycle assessment and economic benefit analysis

In this study, we analyzed the total carbon dioxide (CO_2) emissions from the production of 1 t of cementitious material, considering the comprehensive "cradle-to-gate" perspective of life cycle assessment. However, data inventory, specifically for hazardous waste materials (i.e., MSWI FA, BFS, and DFG) generated by industrial by-products from steel mills and power plants, is unavailable. Therefore, for this study, we excluded the production inputs and outputs associated with BFS and DFG. We focused solely on quantifying CO_2 emissions related to the procurement of raw materials for cementitious material production

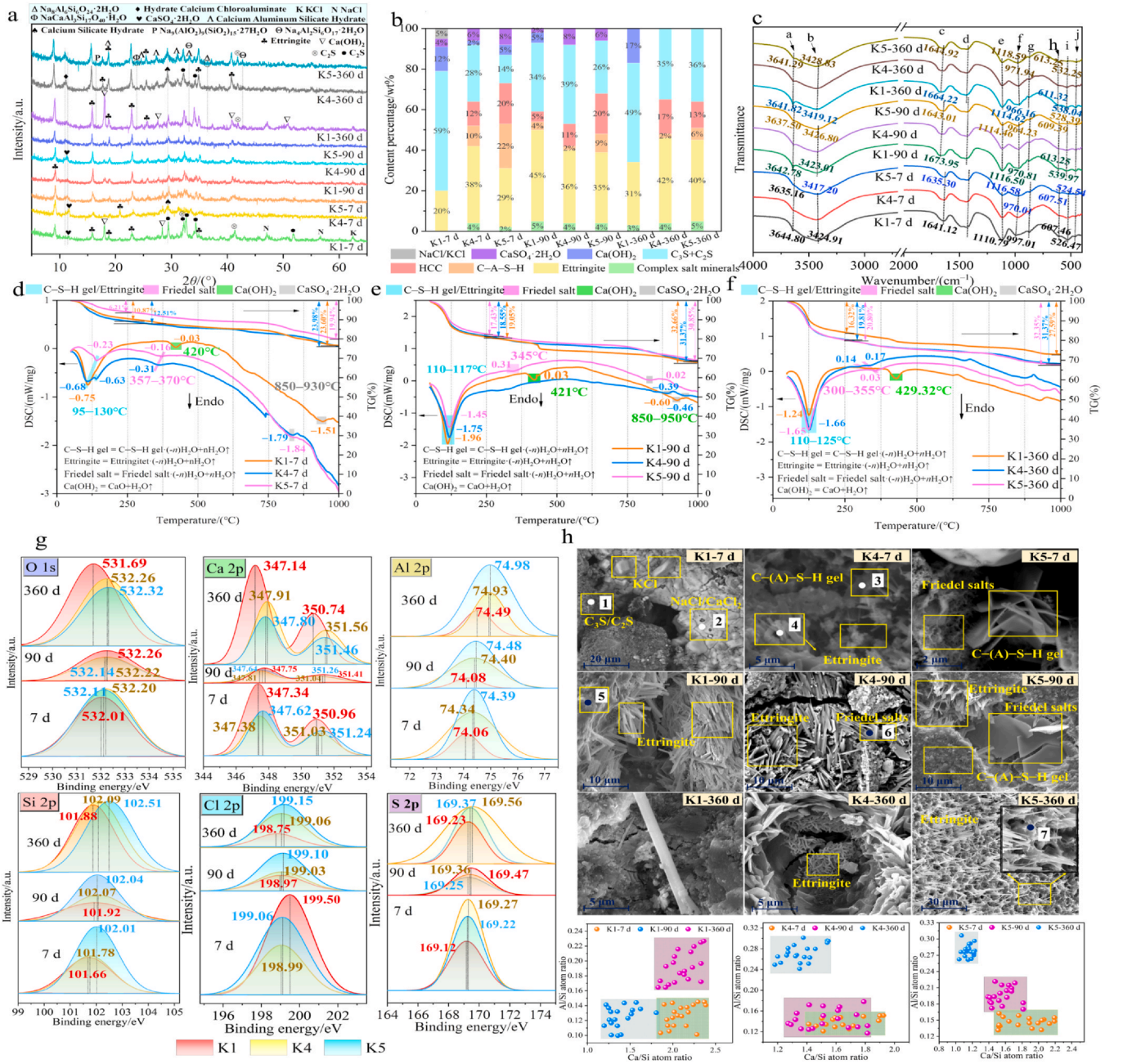

Fig. 3. Microscopic mechanism analysis of K1, K4, and K5 at 7, 90, and 360 d, respectively: (a) qualitative analysis using X-ray diffraction (XRD); (b) semi-quantitative analysis of the crystalline phase using XRD; (c) analysis of hydrated product species and their chemical bonds in K1, K4, and K5; (d–f) weightless hydration products and weightless substances corresponding to K1, K4, and K5 at varying temperatures; (g) variations in binding energies and corresponding fitting curves of the O, Ca, Al, Si, Cl, and S orbitals of the K1, K4, and K5 samples; (h) micromorphological structures of K1, K4, and K5 at various hydration times. The change in the Ca/Si atomic ratio and Al/Si atomic ratio in the gel region corresponds to the transformation of hydrate product types.

based on established performance standards. The CO_2 emissions for cement were calculated using data obtained from a sample of 30 production lines across 18 cement plants in China, as documented in the China Life Cycle Inventory (CNMLCA 2012) [30]. Data on other solid waste raw materials were obtained from the Ecoinvent database; meanwhile, the inventory for BFS was obtained from Paulu *et al.* [31], and the inventory for DFG was obtained from Li *et al.* [32]. The quantification of CO_2 emissions associated with MSWI FA was derived from the generation of CFA in coal-fired processes and landfills, as reported in the aforementioned studies [31,32].

The economic benefit analysis of cementitious materials was conducted using field data on solid waste raw materials obtained locally, along with quotations from e-commerce platforms in the region. Table S8 provides a comprehensive summary of the economic assessment calculations for each cementitious material, considering several factors, such as product benefits, carbon tax/credit, savings in disposal fees, and overall economic gains.

3. Results

3.1. Mechanical properties

Fig. 2(a) compares the compressive strength of test blocks cured for 3, 7, 28, 90, 180, and 360 d and shows that replacing cement with BFS can enhance the compressive strength of solidified blocks. The compressive strength initially increases with the curing period but

subsequently decreases. All test blocks cured for 3 d exceeded 20 MPa. K4, with 60% BFS replacement, exhibited the highest compressive strength after 3, 7, and 180 d of curing, attaining 46.20, 44.10, and 45.18 MPa, respectively. K5 achieved the highest compressive strength (41.49 MPa) after 360 d, and K5 exhibited a stable compressive strength range of 27.65–47.26 MPa across hydration ages of 3–360 d. Previous studies [28,33,34] have shown that the compressive strength of a solidified body can indicate the compactness of its internal structure. Moreover, the combination of the observed leaching concentration and the morphological analysis can reflect the S/S effect and migration transformation law of heavy metals.

3.2. Leaching tests

Fig. 2(b–f) show the leaching concentrations of heavy metal ions, which indicate that the MSWI FA raw material exceeded the standard. However, for the K2–K5 test blocks, the leaching concentrations of heavy metal ions after various hydration periods were below the drinking water standard. By contrast, the K1 test block had a high Pb concentration that exceeded the drinking water standard at all hydration periods, thus posing the risk of leaching. Morphological analysis (Fig. S2) revealed that, after hydration, the residual Pb content of K1–K5 increased (> 88%), with K1 having a higher proportion of oxidizable and reducible states than K2–K5. As the amount of BFS replacement increased, the leaching concentration of Pb decreased significantly, thus significantly influencing the solidification of Pb. The S/S effect was similar to the variations in compressive strength (Fig. 2(a)), and the leaching concentration of heavy metals in the test block with high compressive strength was generally low, meeting the groundwater Class III standard and even the groundwater Class II water quality standard for certain ages. After 90 d of hydration, K3 exhibited the highest strength with a relatively lower leaching concentration of heavy metals. K5 exhibited a super-stable comprehensive heavy metal S/S effect, and the content of multi-heavy metal residue states in the later stages of hydration (K5-360 d) was greater than that of K1. The pH values of the leachate at different ages of K1–K5 are shown in Fig. 2(g), and the alkalinity conditions required for the hydration of the cementitious system were satisfied. The pH of K5 was relatively stable across all hydration ages, indicating a stable alkaline environment in its cementitious system and providing a basis for the stability of hydration products in the later stage.

The dioxin toxic equivalent concentrations in K1 and K5 were 33 and 25 ng-TEQ/kg, respectively, indicating that K5 had a higher S/S capability for organic poisons than K1. In addition, both K1 and K5 met the standard limit of 50 ng-TEQ/kg in the technical specification for controlling MSWI FA pollution in domestic waste incineration (HJ 1134–2020). Table S5 provides more details.

3.3. Hydration microscopic analysis of the paste samples

Fig. 3(a) and (b) shows the XRD analysis results of K1, K4, and K5 at different ages. K1-7 d had the highest proportions of C_3S, C_2S, and $Ca(OH)_2$, while K4-7 d had the highest proportion of ettringite. K4-7 d and K5-7 d exhibited characteristic peaks of complex salt minerals, and K5-7 d had a relatively high proportion of C–A–S–H gel and Friedel's salt. $Ca(OH)_2$ in K1 reappeared after 360 d, and the gypsum peaks disappeared in all three samples. K4 and K5 generated more aluminum-containing crystal phases than K1. TG–DSC analysis showed that K1 and K4 had higher endothermic peaks than K5 at 7 d, and K5-360 d had the highest endothermic peak. K4 and K5 exhibited weak Friedel's salt endothermic peaks; meanwhile, $Ca(OH)_2$ endothermic peaks appeared in K1 at various ages. Based on the vibration absorption peaks of the C–(A)–S–H gel associated with Si–O bonds at locations f, g, h, i, and j, the highest degree of C–S–H gel polymerization was observed in K1-90 d. After hydration for 360 d, as the BFS content increased, the wavenumber shifted to high wavenumbers (i.e., 966.16 cm^{-1} for K1-360 d and 971.94 cm^{-1} for K5-360 d). The adjacent coordination of K5 with Al replacing Si [35] in $[SiO_4]^{4-}$ indicated that K5 contains more types of gel-like hydration products than K1. The information regarding the position of chemical bond peaks can be found in Table. S9. The TG–DSC spectra of K1, K4, and K5 after hydration for 7, 90, and 360 d are depicted in Fig. 3(d–f), and the weightless hydration products, along with the weightless substances corresponding to different temperatures are listed in Table S10. The endothermic peak is primarily concentrated at 110 °C and is caused by the dehydration of ettringite and the C–S–H gel [36]. Moreover, the endothermic peaks of K1-7 d and K4-7 d were significantly higher than that of K5-7 d, corresponding to weight losses of 10.87%, 12.51%, and 6.21%, respectively. As the curing age increased, the endothermic peak of K5-360 d gradually increased to − 1.65 mW/mg, the highest endothermic peak of K1-90 d was − 1.96 mW/mg, and the endothermic peak of K1-360 d significantly decreased. K4 and K5 exhibited weak Friedel's salt endothermic peaks at ~357 to 370 °C at various ages [37], whereas $Ca(OH)_2$ endothermic peaks appeared in K1 at 420 °C at various ages [36]. This finding is consistent with the results of the highest $Ca(OH)_2$ content in K1 (i.e., 12wt% for K1-7 d, 5wt% for K1-90 d, and 17wt% for K1-360 d) compared with K4 and K5 at the same period as XRD quantification, indicating that cement-based K1 contained multilayered $Ca(OH)_2$ in the hydration products generated in the later stages of hydration.

Table S11 shows the variations in the binding energies of the O, Ca, Al, Si, Cl, and S orbitals in samples K1, K4, and K5, as well as the semiquantitative analysis data for the corresponding curve fitting areas. The predominant form of O atoms in the sample was oxygen bridge bonds. The O 1s binding energy of K4-7 d had the largest peak area and the highest number of oxygen bridge bonds compared with those of K1 and K5. After 90 d, the O 1s binding energy of K1 increased to a maximum of 532.26 eV. After 360 d, the O 1s binding energy of K5 increased to 532.32 eV, indicating continuous polymerization of oxygen bridge bonds, whereas the O 1s binding energy of K1 decreased to 531.69 eV, with a tendency for O atoms to convert into non-oxygen bridge bonds [35]. The largest area of the fitted peak of Ca 2p was observed in K1-7 d, whereas the highest binding energy of the Ca 2p main peak was observed in K5-7 d. The Ca 2p binding energy and fitted peak area of K4-90 d increased to their maximum. The Al 2p binding energies increased as the BFS substitution increased, indicating the generation of hexacoordinated Al in the system. The Si 2p binding energy and corresponding peak area increased as BFS replacement and hydration time increased [37], with K5-360 d producing more stable silicate species than K1-360 d. K1-360 d showed reduced chloride binding capability, whereas K5-360 d exhibited stable chloride binding capability and a higher degree of polymerization. The S 2p binding energy of K1-90 d was greater than those of K4-90 d and K5-90 d, whereas the S 2p binding energy of K1-360 d decreased and those of K4-360 d and K5-360 d increased. The hydration reaction of the BFS-based material continued to generate ettringite with the increase in the degree of polymerization in the later stages of hydration [28].

Fig. 3(h) and Table S12 present the micromorphological structure and hydration products of K1, K4, and K5 after hydration for 7, 90, and 360 d. K1-7 d contains higher levels of C_2S/C_3S and chlorine salts with high crystallinity, such as NaCl, KCl, and $CaCl_2$. K4-7 d shows that Ca/Si atomic ratio = 11.85/13.02 < 1, and the ontents of S (7.11at%), Al (3.9at%), and Ca (18.67at%) at Site 4 were higher than those of the other elements. Sites 3 and 4 represent the hydration products of the C–(A)–S–H gel and ettringite, respectively. K5-7 d shows flaky Friedel's salt staggered on top of each other, with visible flocculation of the C–(A)–S–H gel. In K1-90 d, numerous clusters of ettringite were observed, including a gel-like substance (inferred to be the C–S–H gel) at five sites, which was closely cemented with numerous ettringites and a dense structure. In K4-90 d and K5-90 d, the chlorine-containing complex salts were relatively stable, and Friedel's salt was cemented with the increase in the ettringite content, where the chloride salt exhibited a higher binding capacity than that in K1-90 d. The structure in

K1-360 d loosened, the crystalline phase became coarse, and microcracks appeared. K4-360 d and K5-360 d exhibited numerous needle-like ettringites cemented with the gel substance, and the structure was denser than that of K1-90 d. EDS analysis of K5-360 d Site 7 indicated higher elemental contents of Na (5.47at%), Al (8.63at%), Ca (19.52at %), and Si (20.12at%), which were attributed to the formation of the sodium–aluminum–silicate–hydrate (N–A–S–H) crystal phase. In the later stages of hydration, the hydration products of K5-360 d exhibited higher durability, stability, and structural compactness than those of K1-360 d.

EDS analysis was conducted on the gel regions of the K1, K4, and K5 samples after hydration for 7, 90, and 360 d to determine the transformation law and degree of polymerization between the gels. The Ca/Si atomic ratios in K4-7 d and K5-7 d were lower than that in K1-7 d, i.e., ranging from 1.41 to 1.92 and from 1.51 to 2.19, respectively. As BFS substitution increased, the Al/Si atomic ratio gradually increased, indicating that the strongest conversion trend of the C–S–H gel into the C–A–S–H gel occurred in K5-7 d. The degree of polymerization of Si in K1, K4, and K5 increased with the decrease in the Ca/Si atomic ratios in K1-90 d, K4-90 d, and K5-90 d [16,38]. The Ca/Si atomic ratio in

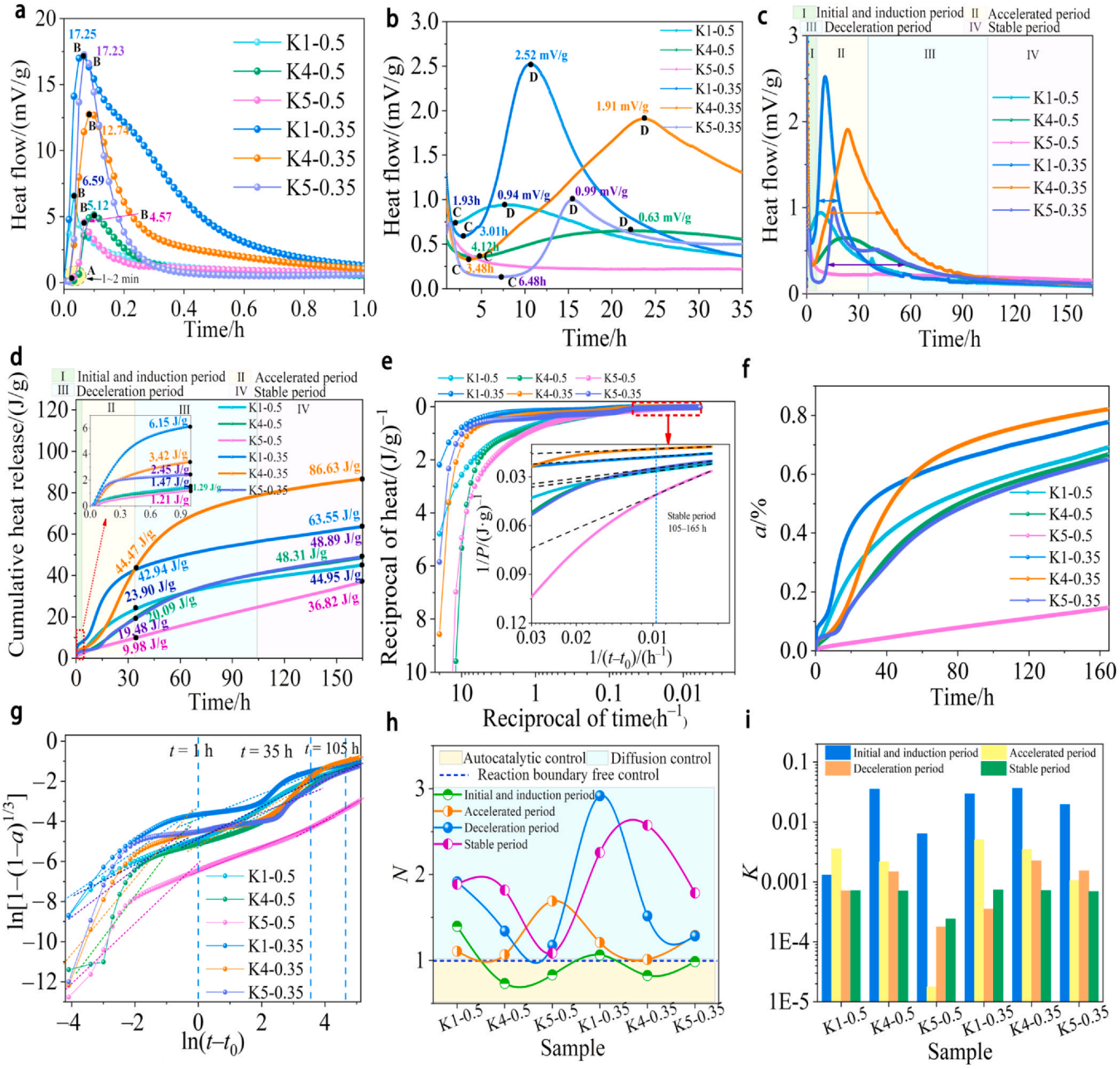

Fig. 4. Hydration heat release of K1, K4, and K5 at a WTB ratio of 0.35–0.5 for 168 h (7 d) during the hydration process: (a) variation in hydration heat release within 1 h of the hydration process; (b) variation in hydration heat release for 1–35 h during the hydration process; (c) variations in hydration exothermic heat releases for 168 h (7 d) during the hydration process; (d) accumulated hydration heat release versus total accumulated heat release for 168 h (7 d) during the hydration process; (e) fitting curves of final heat release (P_m) and half-life (t_∂) according to Knudson's equation ($\frac{1}{P} = \frac{1}{P_m} - \frac{t_\partial}{P_m(t-t_0)}$) of hydration kinetics; (f) variation in hydration degree for 168 h (7 d) calculated according to Eq. (S2): $a = \frac{P}{P_m}$; (g) curve of the relationship between $\ln[1-(1-a)^{1/3}]$ and $\ln(t-t_0)$; (h) variations in hydration reaction mechanism constant N obtained by fitting the curve of the relationship between $\ln[1-(1-a)^{1/3}]$ and $\ln(t-t_0)$ at various stages; (i) variations in reaction velocity constant K obtained by fitting the curve of the relationship between $\ln[1-(1-a)^{1/3}]$ and $\ln(t-t_0)$ at various stages. All equations and variable definitions could be obtained in Supplementary Information.

K1-360 d was the highest compared with those in K4-360 d and K5-360 d. By contrast, in K4-360 d and K5-360 d, the Ca/Si atomic ratios were lower, and the silicate hydration products exhibited a higher degree of polymerization than cement-based K1 with a gradual increase in the Al/Si atomic ratio.

3.4. Hydration heat tests and results

Fig. 4 shows the hydration heat release data of K1, K4, and K5 for 168 h (7 d) at various WTB ratios. Fig. 4(a) shows the hydration heat variation within 1 h at WTB ratios of 0.35 and 0.5. The exothermic peaks occurred within 1–2 min, with the first peaks of K1-0.5, K4-0.5, and K5-0.5 occurring at approximately 2.5, 5, and 6 min, respectively. The exothermic rates of K1-0.5, K4-0.5, and K5-0.5 were 6.59, 5.12, and 4.57 mV/g, respectively. The initial exothermic peak of K1-0.35 was delayed by 5 min, but the exothermic rates of K1-0.35, K4-0.35, and K5-0.35 increased to 17.25, 12.74, and 17.23 mV/g, respectively. Fig. 4(b) shows the thermal variation of hydration within 35 h. The maximum hydration heat release rate was 0.94 mV/g for K1-0.5 and 0.63 mV/g for K4-0.5. The start times of the acceleration periods of K1-0.35,

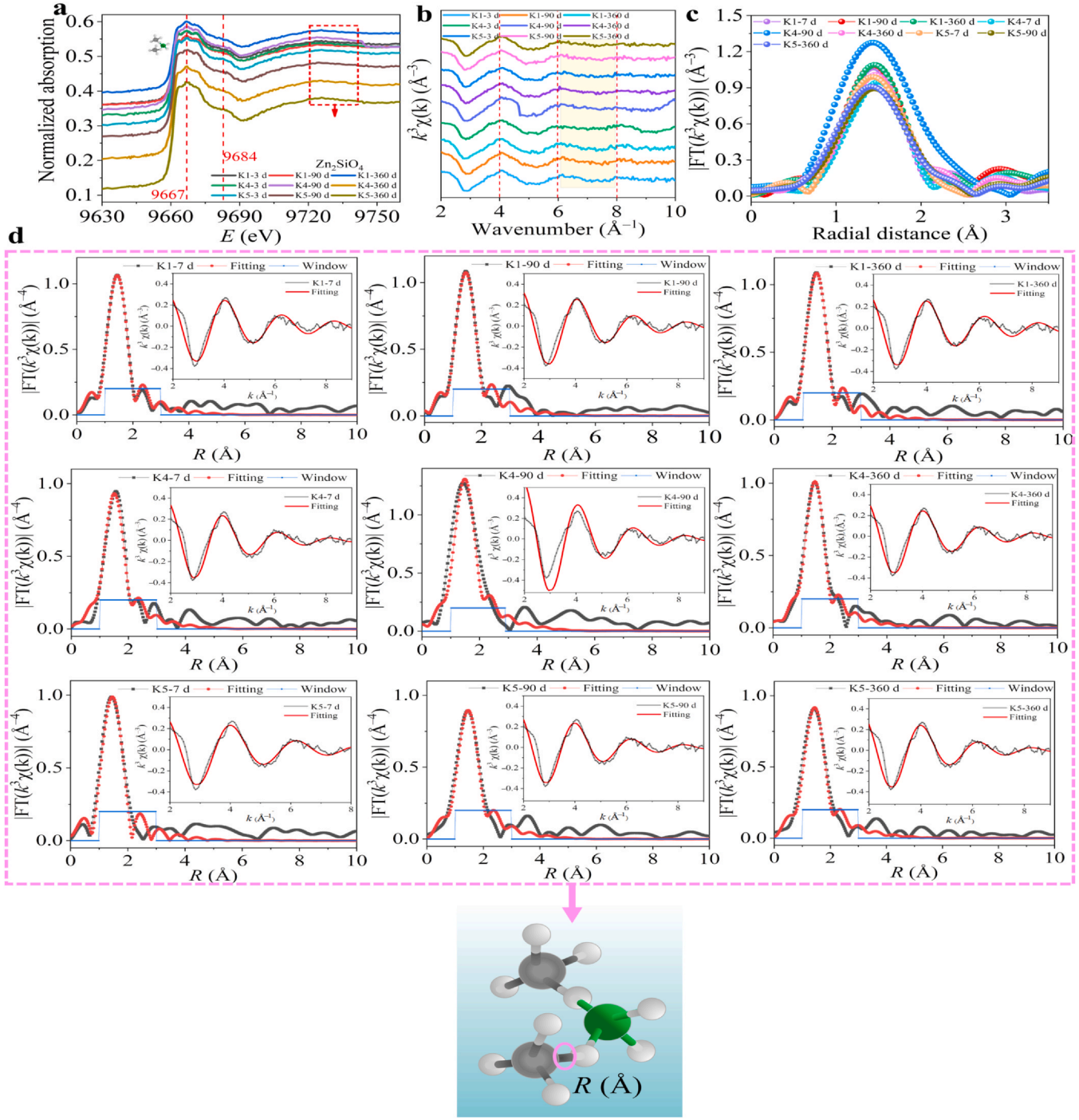

Fig. 5. Zn LIII-edge X-ray absorption fine structure spectra of K1, K4, and K5: (a) Zn LIII-edge X-ray absorption near-edge structure (XANES); (b) Zn LIII-edge $k^3\chi(k)$ extended X-ray absorption fine structure (EXAFS); (c) Fourier transform magnitude of Zn LIII-edge EXAFS spectra of the K1, K4, and K5 samples; (d) fitting results of the corresponding RSF spectra of the Zn–O shell backscattering paths expected with Zn_2SiO_4. The black and red lines denote the experimental and fitted data, respectively.

K4-0.35, and K5-0.35 were 3.01, 3.48, and 6.48 h, with maximum heat release rates of 2.52, 1.91, and 0.99 mV/g, respectively [39,40]. Only K1-0.5 and K4-0.35 showed exothermic peaks in the hydration deceleration period from 35 to 105 h, with maximum exothermic rates of 0.41 and 0.74 mV/g, respectively. The total heat release decreased as the BFS replacement increased under the same WTB ratio, and the cumulative heat release of K1-0.5, K4-0.5, and K5-0.5 was 1.47, 1.29, and 1.21 J/g, respectively. At a WTB ratio of 0.35, the cumulative heat release increased, and the total heat dissipation of K1-0.35, K4-0.35, and K5-0.35 increased to 42.94, 44.47, and 19.48 J/g, respectively. A WTB ratio of 0.35 was more conducive to improving the hydration heat of BFS-based cementitious materials [41]. After a hydration period of 35 h, the total heat release of K4-0.35 exceeded that of K1-0.35, and the total heat release of K1-0.35, K4-0.35, and K5-0.35 was 63.55, 86.63, and 48.89 J/g, respectively (Fig. 4(d)).

Fig. 4(e) and Table S13 indicate that longer hydration periods result in more consistent final heat release, and a linear relationship only exists after 105 h. The final exothermic P_m and the fitted half-life data t_∂ can be used to evaluate the long half-life of K5-0.5 (967.5604 h). Decreasing the WTB ratio from 0.5 to 0.35 considerably reduced the half-life t_∂ of K4 and K5 by 56.83% (83.4252–36.0127 h) and 90.82% (967.5604–88.8520 h), respectively. The hydration degree of each sample can be evaluated using Eqs. (S1) and (S2). The hydration degree of K4-0.35 exceeded that of K1-0.35, attaining a maximum of ~0.8 at 168 h. The values of N and K were calculated by fitting them using Eqs. (S3) and (S4), as presented in Fig. 4(g) and Table S14, and the specific variations in N and K are plotted in Fig. 4(h) and (i), respectively. In the induction stage, K4 and K5 ($N < 1$) were predominantly controlled by an automatic catalytic reaction, K1-0.5 ($N = 1.39811 > 1$) was controlled by diffusion, and K1-0.35 ($N = 1.06340$) was freely controlled by the reaction boundary. During the acceleration phase, K4 was freely controlled by the reaction boundary, whereas K5 and K1 were primarily controlled by diffusion. The reaction resistance of the cement-based system increased as the WTB ratio decreased from 0.5 to 0.35, and a WTB ratio of 0.35 is more suitable for BFS-based systems. During the deceleration phase, all samples were subjected to diffusion control. The K values of K4 and K5 in the induction period were 10 times those of the other reaction stages.

3.5. XAFS analysis of Zn

Fig. 5(a) shows that, because of the low content of heavy metals in the solidified body, only the near-edge XAFS of Zn can be measured. The morphology of the nine samples was similar, indicating a consistent Zn coordination environment.

The main peak position was at A (~9666 eV), and the weak peak at B (~9684 eV) was representative of Zn_2SiO_4 [42]. The radial structure function of the Zn ion coordination layer showed the peak ion radius R value of ~1.5, which denoted the Zn–O bond [23]. The k-space function curve showed peak patterns surrounding wavenumbers 4, 6, and 8, consistent with Zn_2SiO_4. After 7 d of hydration, the Zn residue content of K1–K5 was > 90%. The results of the single-shell fitting process and the Zn–O bond length of Zn_2SiO_4 are depicted in Fig. 5(d) and Table S15. The mass fractions of Zn residue, oxidizable, reducible, and acid-extractable states in the MSWI FA raw material were 51%, 31%, 12%, and 6%, respectively, as shown in Fig. S1.

As shown in Table S15, the first coordination layer of Zn in the solidified sample is coordinated with three O atoms. The σ^2 values of K4 and K5 were higher than that of K1, indicating that the Zn_2SiO_4 compound structure in BFS-based cementitious materials was more complex than that in cement-based materials. The Zn–O coordination bond lengths of K1 and K5 increased as the hydration age increased (i.e., 1.93531–1.95226 Å for K1 and 1.95999–1.97594 Å for K5). In K4, the Zn–O bond length decreased with the increase in the hydration age. However, the bond lengths of K4 and K5 were within the range of 1.95500–1.98037 Å, which were longer than those at all ages of K1, particularly in the later stages of hydration (360 d). With the increase in the BFS substitution, the Zn–O bond lengths of K1-360 d, K4-360 d, and K5-360 d gradually increased to 1.95226, 1.95500, and 1.97594 Å, respectively.

4. Discussion

4.1. Advantages of the BFS–MSWI FA–DFG cementitious system

The experiments showed that low-clinker or clinker-free cementitious systems can be prepared using BFS, an aluminosilicate synergistically excited by MSWI FA and DFG, instead of cement clinker as the main component. Replacing cement with BFS significantly improved the S/S effect on the strength, leaching concentration, and heavy metal status of the cementitious system. K5 had the highest compressive strength of 41.49 MPa on the 360th day, and its macrostrength durability and stability were the highest. The leaching concentrations of various heavy metals in the K2–K5 samples were lower than the drinking water standard, and some were even below the groundwater Class II standards, achieving the role of super S/S. Zn can be detected through synchrotron radiation and is mainly solidified by silicate substances, converting into the residual state of the Zn_2SiO_4 silicate phase. In the later stage of 360 d of hydration, the residual state of Zn was still 94%, and the S/S effect was relatively stable. The Zn ions can be more easily trapped in the silicon–oxygen tetrahedral network of the C–S–H gel and ettringite to balance the charge or replace the trapped Ca ions in its lattice, forming a complex salt precipitation of larger molecules, solidifying the Zn ions [42–45], and preventing their leaching.

To investigate the structural regulation of hydration products, we used a WTB ratio of 0.5 for cement systems and 0.35 for solid-waste-based systems for thermodynamic comparison. The WTB ratio of 0.5 resulted in a faster onset time and higher exothermic rate of cement-based K1 [40]. By contrast, the WTB ratio of 0.35 was more conducive to shortening the induction period of BFS-based K4 and K5, resulting in a higher exothermic rate during the acceleration period. K4-0.35 also had a higher total hydration heat release than K1-0.35 in the later stages of hydration [46]. The acceleration of the hydration reaction rates of K4 and K5 increased the number of hydration products and shortened the coagulation time of the cementitious material, thus increasing the compressive strength [47]. In addition, the glass phase of BFS dissociated in an alkaline environment, continuously supplying the silicate and aluminate ions required for hydration products during the peak of the hydration reaction [28,48], resulting in wider peaks of the exothermic rates of K4-0.35 and K5-0.35 than that of K1-0.35.

During the induction period, the BFS-based material was controlled by the automatic catalytic reaction, whereas K1-0.5 was controlled by diffusion, and K1-0.35 was freely controlled by the reaction boundary. The hydration kinetics parameter K represents the chemical reaction rate of cementitious materials during the production process. The K value enables us to characterize the increase in the concentration of generated substances per unit time, thereby ensuring the enhancement of subsequent strength performance. The K value of the BFS-based materials was 10 times higher during the induction period, indicating a faster chemical reaction rate. During the acceleration period, K4 was freely controlled by the reaction boundary at both WTB ratios of 0.35 and 0.5, while K5 and K1 were mainly controlled by diffusion.

For the corresponding WTB ratios, the N and K values of the cement-based materials were larger than those of the BFS-based materials, with the N value indicating reaction resistance [24,49]. Decreasing the WTB ratio from 0.5 to 0.35 increased the N value of cement-based K1 (i.e., 1.10664 at the WTB ratio of 0.5 and 1.20944 at the WTB ratio of 0.35) and increased the N values of BFS-based K4 and K5, indicating that the reaction resistance of cement-based materials increased, whereas that of BFS-based materials decreased. During the deceleration period, the BFS-based materials were controlled by diffusion, except for K5-0.5, because the BFS-based materials (K4 and K5) contained a higher

proportion of glassy silica tetrahedra [SiO_4] and alumina tetrahedra [AlO_4]. The reactive elements Si and Al continuously leached out during the passive hydration process within 168 h, consistently participating in the formation of hydration products, such as ettringite and C–(A)–S–H gel in the system. The *N* values of K1-0.5 and K1-0.35 during the acceleration period were lower than those of K5-0.5 and K5-0.35, indicating that the hydration resistance of cement-based materials was lower during the acceleration period than that of BFS-based materials. However, the denser hydration product layer hindered hydration from intensifying [41,49], reducing the strength of the cement-based material K1 after 168 h (7 d) of hydration compared with the BFS-based materials K4 and K5. A lower WTB ratio, while meeting fluidity, can decrease the porosity and increase the overall performance of the cementitious material.

4.2. Characteristics of the BFS–MSWI FA–DFG cementitious system

Microscopic analysis revealed that, during the 7-d hydration stage, K1 exhibited high calcium characteristics because of the higher contents of C_2S and C_3S in the cement clinker [28,50], resulting in a higher Ca/Si atomic ratio (1.86–2.39) than K4 and K5 (K4 = 1.41–1.92 and K5 = 1.51–2.19; Fig. 3(h)). The hydration reaction in the cementitious system, where MSWI FA and DFG synergistically excite BFS, is somewhat different from the active hydration of cement-based materials and can be referred to as "passive" hydration. Under alkaline conditions, a large amount of CaO is dissolved in MSWI FA, generating $Ca(OH)_2$ and rapidly promoting the depolymerization of amorphous aluminosilicate in BFS. Depolymerized active $[AlO_4]^{5-}$ co-excites with Ca^{2+}, SO_4^{2-} (provided by DFG), and alkalis to generate ettringite complex salt minerals (Eq. (1)) and Friedel's salt (Eq. (2)) under alkaline conditions. The interlaminar anions of Friedel's salt exhibit exchangeability [51], aiding in the removal of harmful ions and organic contaminants (Fig. 6).

Previous studies [28,29,51] have reported the competitive relationship between Cl^- and SO_4^{2-}, where the presence of more SO_4^{2-} results in the formation of the ettringite phase and the presence of more Cl^- results in the formation of Friedel's salt to achieve a balance. After depolymerizing the active $[AlO_4]^{5-}$ in BFS, the amorphous phase of BFS drives the depolymerization of $[SiO_4]^{4-}$ and forms a C–S–H gel with a lower Ca/Si atomic ratio by reacting with $Ca(OH)_2$ (Eq. (3)). The active Al in BFS replaces Si in the C–S–H gel silicon chain, forming a C–A–S–H gel with an Al/Si atomic ratio of 0.10–0.16 (Eq. (4)). Increasing the BFS content promotes the conversion of the C–S–H gel into the C–A–S–H gel. SEM analysis showed an increase in the formation of flaky Friedel's salt with the increase in the BFS content, and XPS analysis confirmed the trend of salt minerals forming hexacoordinated Al in the system. XRD analysis of K1-7 d revealed the presence of NaCl and KCl salts, which resulted in poor chlorine salt binding compared with the BFS-based materials.

$$3Ca(OH)_2 + Al_2O_3 + 3(CaSO_4{\cdot}2\,H_2O) + 23H_2O \rightarrow 3CaO{\cdot}Al_2O_3{\cdot}3CaSO_4{\cdot}32\,H_2O \text{ (ettringite)} \quad (1)$$

$$Al_2O_3 + 4CaO + 4NaCl + 7H_2O \rightarrow 2Ca_2Al(OH)_6Cl_2H_2O \text{ (Friedel's salt)} + 4Na^+ \quad (2)$$

$$Ca(OH)_2 + (n-1)H_2O + SiO_2 \rightarrow CaO{\cdot}SiO_2{\cdot}nH_2O \text{ (C–S–H)} \quad (3)$$

$$Ca(OH)_2 + (n-1)H_2O + Al_3O_2 + SiO_2 \rightarrow CaO{\cdot}SiO_2{\cdot}Al_2O_3{\cdot}nH_2O \text{ (C–A–S–H)} \quad (4)$$

$$(n-1)H_2O + Al_3O_2 + SiO_2 + Na_2O \rightarrow Na_2O{\cdot}SiO_2{\cdot}Al_2O_3{\cdot}nH_2O \text{ (N–A–S–H)} \quad (5)$$

$$Ca(OH)_2 + (n-1)H_2O + Al_3O_2 + SiO_2 + Na_2O \rightarrow Na_2O{\cdot}CaO{\cdot}SiO_2{\cdot}Al_2O_3{\cdot}nH_2O \text{ (N–(C)–A–S–H)} \quad (6)$$

After 90 d of hydration, K1-90 d not only had a higher degree of polymerization of ettringite and C–S–H/C–A–S–H gel than K4-90 d and K5-90 d but also had the largest total hydrated product loss (Fig. 3(e)). The O 1s binding energy (532.26 eV) and peak area of K1-90 d were also the largest (Fig. 3(g)), and SEM analysis revealed tightly cemented clustered C–S–H gels with ettringite in K1-90 d, which had a dense structure. However, EDS analysis showed that K4-90 d and K5-90 d produced complete Friedel's salt, along with the increase in the amount of aluminite cemented with Friedel's salt. After 360 d of hydration, K1-360 d showed a loose and cracked structure under SEM (Fig. 3(h)), K4-360 d showed ettringite clusters with cracks, and K5-360 d had an extensive amount of needle-like calcium alum cemented with the gel substance, resulting in a higher structural compactness than K1-360 d.

After 360 d, K4 and K5 had lower Ca/Si atomic ratios of 1.18–1.54 and 1.04–1.23, respectively, whereas K1 maintained a higher Ca/Si atomic ratio of 1.83–2.36. Based on the Ca/Si atomic ratio variation range, K1 had a crystalline phase similar to jennite ($Ca_9Si_6O_{32}H_{22}$), whereas the species of C–S–H gel in K4 and K5 belonged to jennite in the early stage (7 d). After 360 d, K4 and K5 had Ca/Si atomic ratios in the range of 1.18–1.54 and 1.04–1.23, respectively, transitioning to 1.4-nm tobermorite ($Ca_5Si_6O_{26}H_{18}$) with a higher degree of polymerization with the increase in the hydration age.

With the variation in the Ca/Si atomic ratio, the C–S–H gel transformed into its polymerized structure, as shown in Fig. 6(a), and the silicon–oxygen tetrahedral chain structure of each C–S–H gel is composed of three Si tetrahedral repeats [38]. As Ca/Si atomic ratio increases, a portion of the Si tetrahedra in the third position acting as a bridge disappears [38], thereby detaching Ca from the silicon chain in the form of $Ca(OH)_2$. BFS contains more Al_2O_3 than the cement clinker, and Al/Si atomic ratio increases with the increase in the BFS content at each hydration time. In particular, in the later stages of hydration (360 d), the Al/Si atomic ratio values of K1-360 d, K4-360 d, and K5-360 d were 0.16–0.23, 0.24–0.30, and 0.26–0.31, respectively. In addition, the bending vibration peak *i* and absorption peak *j* of the C–(A)–S–H gel in the FTIR analysis shifted to low wavenumbers with the increase in the BFS content at the same age. Combined with the increase in the BFS content and hydration time in the XPS analysis (Fig. 3(g)), the binding energies and corresponding peak areas of Al 2p and Si 2p increased, which proved that the degree of polymer crystallization of the C–A–S–H gel in the BFS-based material increased with the increase in the hydration time [34,52,53]. Based on the XRD analysis, K4 and K5 formed sodium–(calcium)–aluminum–silicate–-hydrate (N–(C)–A–S–H) and N–A–S–H phases. When the degree of polymerization of C–A–S–H gel substances increases (Ca/Si atomic ratio gradually decreases), a large amount of soluble Na^+ contained in MSWI FA enters the chain structure of silicon (aluminum) oxygen tetrahedron, where the C–A–S–H gel changes from chain structure to mesh structure, generating the N–(C)–A–S–H phase (Eqs. (5) and (6)), which is similar to the zeolite-like phase (Fig. 6). The N–(C)–A–S–H class zeolite phase has a more complex structure than the C–(A)–S–H gel, indicating that the porous structure improves the interface structure between hydration products, such as gel and solid particles. This closer connection forms a more integral structure, enhancing the strength of the BFS-based material upon hardening. In addition, the porous structure of N–(C)–A–S–H can improve the capability to solidify harmful elements. The N–(C)–A–S–H phase guarantees the adsorption and curing of harmful substances and the improvement of the strength of cementitious materials. The Na/Ca/Al/Si atomic ratio in the EDS analysis of K5–360 d Locus 7 in SEM was 5.47%/19.52%/8.63%/20.12%, which proved the existence of the N–(C)–A–S–H phase (Table S12). Whether in the early (7 d) or late (360 d) stage of hydration, the transition trend of the C–S–H gel to the C–A–S–H gel was greater than that of the cement-based material, and the network structure of K5 was the N–(C)–A–S–H class zeolite phase at 360 d and contained more types of complex silicate hydration products than K1, which was consistent with the results of the macroscopic strength durability and stability tests.

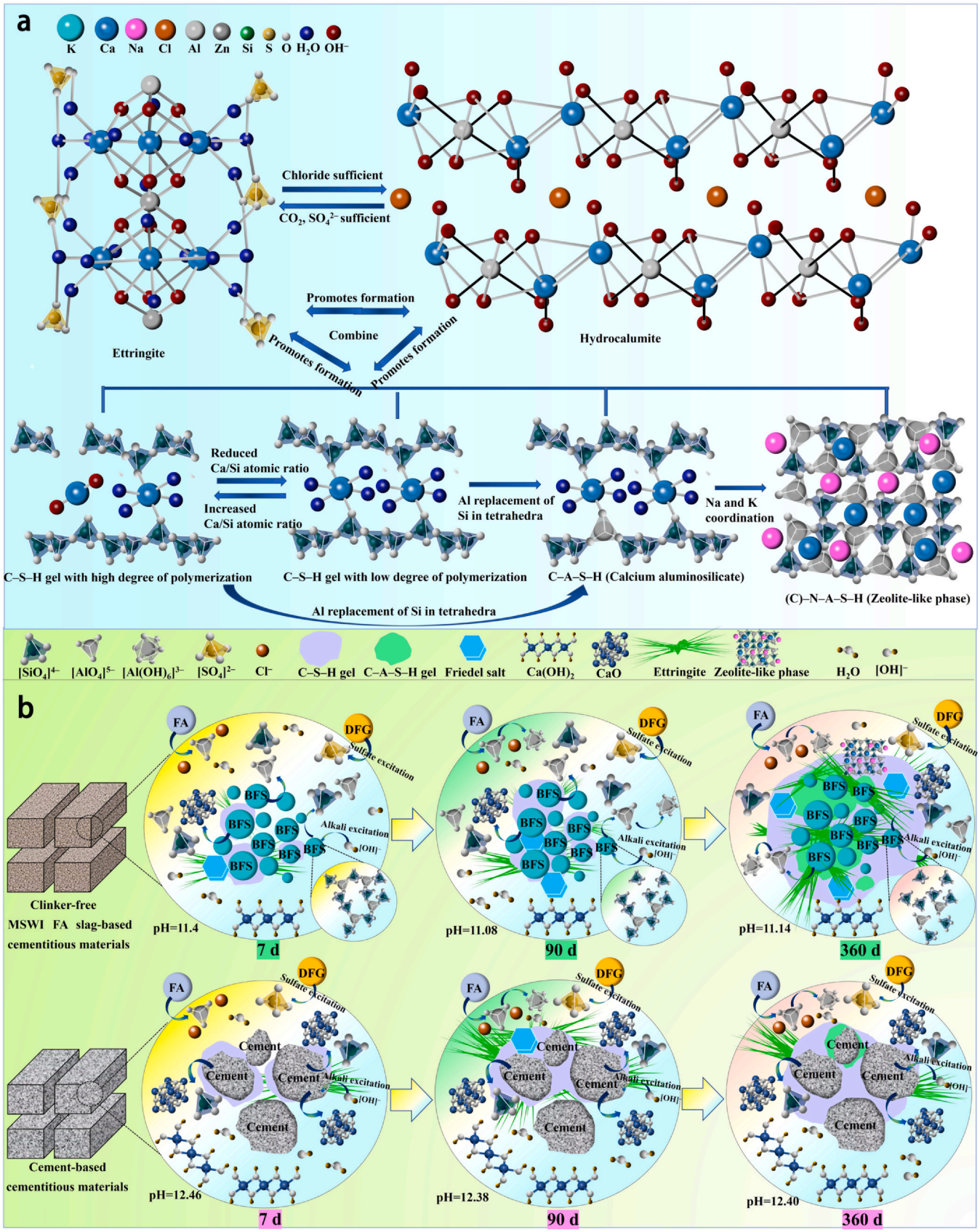

Fig. 6. Hydration mechanisms of BFS-based and cement-based cementitious materials: (a) microstructure transformation mechanism of the hydration products; (b) comparison of the hydration control mechanisms of BFS-based and cement-based cementitious materials.

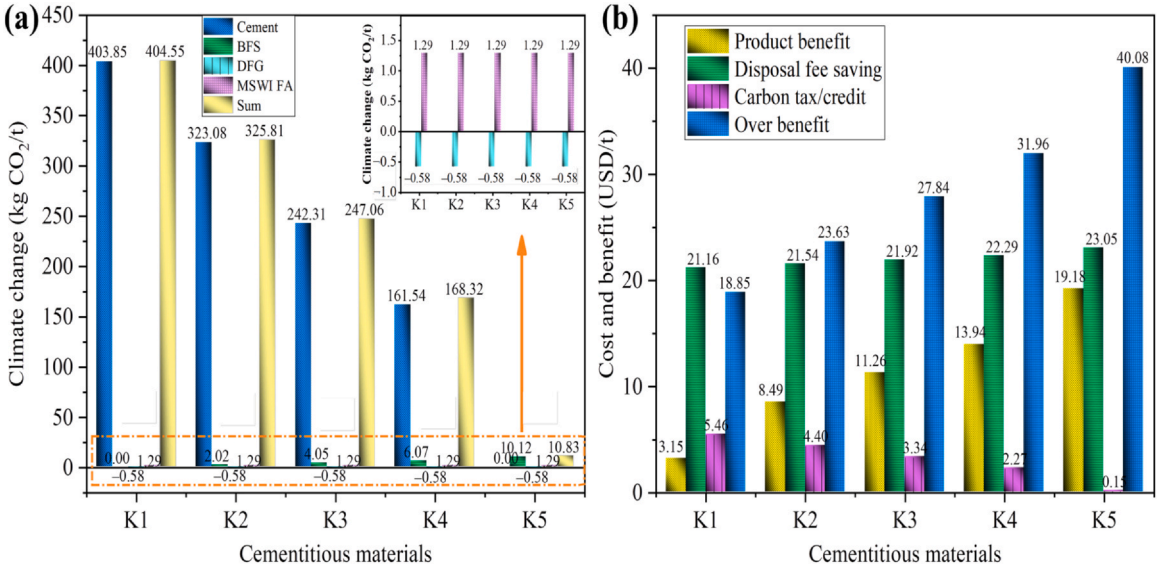

Fig. 7. Life cycle assessment (a) and economic benefit analysis (b) of the clinker-free backfill material MSWI FA containing slag-based cementitious materials.

4.3. Advantages of the BFS–MSWI FA–DFG cementitious system

The proposal of China's new development missions of "carbon peak" in 2030 and "carbon neutrality" in 2060 poses great challenges to the low-carbon transformation and development of the cement industry. Low-carbon and ultralow-cost cementitious materials are an important direction for future development. Our previous research [28,29,36,54] showed that BFS, MSWI FA, CFA, coal gasification slag, ferroalloy slag, and other materials that are mainly based on the glassy amorphous phase aluminosilicate of solid wastes can collaboratively prepare new low-carbon clinker-free or low-clinker cementitious materials through the mechanical rate activation and composite stimulation of MSWI FA, steel slag, desulfurization by-products, calcium carbide slag, and other substances, such as alkalis, sulfates, and chloride salts.

Fig. 7 shows the change in CO_2 emissions in the production of 1 t cementitious materials K1–K5, of which the CO_2 emission in K1 is large (403.85 kg/t) mainly because 70% of the high-content cement comprising cementitious materials, limestone decomposition, and fossil fuel combustion produces 750 kg of CO_2 during the production of 1 t cement. The CO_2 emissions of BFS, DFG, and MSWI FA in the production of 1 t cementitious materials only fluctuated in the range of 0.58–10.12 kg. Therefore, the BFS content of glassy solid waste gradually increased, and replacing cement can continuously reduce CO_2 emissions. CO_2 emissions of K5 solid-waste-based cementitious material were only 10.83 kg/t. The use of solid waste raw materials instead of cement as cementitious materials provides strong low-carbon environmental protection. The calculated data of specific CO_2 emissions are shown in Table S16.

The economic benefit analysis of cementitious materials K1–K5 in this study is mainly divided into product benefit, carbon tax/credit, disposal fee saving, and overbenefit; the specific calculation results are shown in Table S8. Table S8 shows that the cost of cementitious raw materials significantly impacts product benefit, and the price of cement reaches 56 USD/t, whereas the cost of BFS and DFG is 28 and 1.12 USD/t, respectively. The raw material cost of K1 is 30.24 USD/t. An increase in the BFS content reduces the cost of the raw materials, and the raw material cost of K5 is reduced to 15.16 USD/t. The proportion of energy and maintenance costs generated by BFS and DFG pretreatment is lower than MSWI FA, which is < 2.5 USD/t; hence, increasing the BFS content increases the product benefit (calculated by subtracting the operating cost from the set price of 35 USD/t). The product benefit of K1 is only 3.15 USD/t, whereas that of K5 reaches 19.18 USD/t. Disposal fee savings mainly include solid waste storage tax (Environmental Protection Tax Law of the People's Republic of China = 3.5 USD/t) and hazardous waste disposal costs (landfill and cement kiln disposal = 135.8 USD/t). Furthermore, solid-waste-based cementitious materials have the advantages of resource utilization of BFS and DFG solid waste and harmless disposal of MSWI FA hazardous waste, increasing the disposal fee savings with BFS instead of cement (i.e., 21.16 USD/t for K1 and 23.05 USD/t for K5). With the strengthening of global carbon emission reduction and the increasing impact of carbon tax, the gradual increase in BFS content can continuously reduce the carbon tax of cementitious materials, where K1 can be up to 5.46 USD/t and K5 only 0.15 USD/t. Through the overbenefit analysis, the overbenefit of the cementitious material K1 is 18.85 USD/t, and the overbenefit of the solid-waste-based cementitious material increases with the increase in the BFS content. The overbenefit of K5 is the highest at 40.08 USD/t.

Hence, based on the glassy amorphous phase aluminosilicate of solid wastes, the efficient and collaborative use of solid waste in metallurgy, coal power, mining, and other fields is driven by and extensively integrated with mine cementation filling and building material usage. Moreover, with the help of further research on low calcium–silicon ratio cement technology, the potential for carbon emission reduction and economic benefits are considerable.

5. Conclusion

This study showed that K4 exhibited superior compressive strength, with values reaching 46.20, 44.10, and 45.18 MPa after 3, 7, and 180 d of curing, respectively. Meanwhile, K5 exhibited a stable compressive strength range of 27.65–47.26 MPa across hydration ages of 3–360 d. Both K4 and K5 met the drinking water standards for heavy metal leaching, and K5 had a low dioxin content of only 25 ng-TEQ/kg. The characteristics of the materials, such as the Ca/Si and Al/Si atomic ratios, varied with the hydration age, indicating evolving compositions. The addition of a WTB ratio of 0.35 accelerated the hydration reactions, significantly reducing the half-life of K4 and K5. Moreover, this study highlighted the efficient S/S effect of Zn in BFS-based and cementitious materials, forming stable compounds, such as Zn_2SiO_4, and preventing leaching. In addition, the CO_2 emission of K5 solid-waste-based cementitious material was notably low at 10.83 kg/t, yielding a high overbenefit of 40.08 USD/t.

CRediT authorship contribution statement

Siqi Zhang: Writing – review & editing, Project administration, Validation. **Tong Zhao:** Methodology, Writing – original draft. **Huifen**

Yang: Supervision, Resources, Project administration. **Keqing Li:** Supervision, Resources, Project administration. **Wen Ni:** Investigation Supervision, Resources, Project administration. **Zeping Wu:** Investigation. **Jia Li:** Investigation. **Yue Li:** Investigation. **Bo Zhang:** Investigation. **Jiajia Wang:** Investigation. **Runsheng Xu:** Investigation. **Xiaoming Liu:** Investigation. **Pingfeng Fu:** Investigation. **Weihua Cui:** Investigation. **Jun Yao:** Investigation.

Declaration of Competing Interest

The authors declare that they have no known competing financial interests or personal relationships that could have appeared to influence the work reported in this paper.

Acknowledgements

This work was financially supported by the National Key Research and Development Program of China (Nos. 2019YFC1803500 and 2020YFC1910000), Fundamental Research Funds for the Central Universities (Nos. FRF-TP-20-003A1 and FRF-IDRY-20-014). The authors would like to thank Zhongjun Chen, Xiaoyi Zhao, and Yu Gong of the Institute of High Energy Physics, Chinese Academy of Sciences, for their kindly assistance with the X-ray absorption fine structure analysis.

Appendix A. Supporting information

Supplementary data associated with this article can be found in the online version at doi:10.1016/j.gsme.2024.01.001.

References

[1] Y.Y. Zhang, L. Wang, L. Chen, B. Ma, Y.K. Zhang, W. Ni, D.C.W. Tsang, Treatment of municipal solid waste incineration fly ash: state-of-the-art technologies and future perspectives, J. Hazard. Mater. 411 (2021) 125132.
[2] H.X. Zhan, N. Mahyuddin, R. Sulaiman, F. Khayatian, Phase change material (PCM) integrations into buildings in hot climates with simulation access for energy performance and thermal comfort: a review, Constr. Build. Mater. 397 (2023) 132312.
[3] L. Wang, Y.Y. Zhang, L. Chen, B.L. Guo, Y.S. Tan, K. Sasaki, D.C.W. Tsang, Designing novel magnesium oxysulfate cement for stabilization/solidification of municipal solid waste incineration fly ash, J. Hazard. Mater. 423 (2022) 127025.
[4] R. Malviya, R. Chaudhary, Factors affecting hazardous waste solidification/stabilization: a review, J. Hazard. Mater. 137 (1) (2006) 267–276.
[5] Y. Su, J.M. Yang, D.B. Liu, S.C. Zhen, N.X. Lin, Y.X. Zhou, Effects of municipal solid waste incineration fly ash on solidification/stabilization of Cd and Pb by magnesium potassium phosphate cement, J. Environ. Chem. Eng. 4 (1) (2016) 259–265.
[6] M. Nag, T. Shimaoka, A novel and sustainable technique to immobilize lead and zinc in MSW incineration fly ash by using pozzolanic bottom ash, J. Environ. Manag. 329 (2023) 117036.
[7] N. Gineys, G. Aouad, D. Damidot, Managing trace elements in Portland cement–Part I: interactions between cement paste and heavy metals added during mixing as soluble salts, Cem. Concr. Compos. 32 (8) (2010) 563–570.
[8] X. He, Z.Y. Lai, T. Yan, J. Wu, Z.Y. Lu, S.Z. Lv, F. Li, X.L. Fan, Hydration characteristics and microstructure of magnesium phosphate cement in presence of Cu^{2+}, Constr. Build. Mater. 225 (2019) 234–242.
[9] L.N. Lu, C.Y. Xiang, Y.J. He, F.Z. Wang, S.G. Hu, Early hydration of C_3S in the presence of Cd^{2+}, Pb^{2+} and Cr^{3+} and the immobilization of heavy metals in pastes, Constr. Build. Mater. 152 (2017) 923–932.
[10] N.W. Wiesława, T. Barbara, D. Sylwia, The properties of cement pastes and mortars processed with some heavy metal nitrates containing solutions, Procedia Eng. 108 (2015) 72–79.
[11] Q.Y. Chen, C.D. Hills, M. Tyrer, I. Slipper, H.G. Shen, A. Brough, Characterisation of products of tricalcium silicate hydration in the presence of heavy metals, J. Hazard. Mater. 147 (3) (2007) 817–825.
[12] L. Wang, D.A. Geddes, B. Walkley, J.L. Provis, V. Mechtcherine, D.C.W. Tsang, The role of zinc in metakaolin-based geopolymers, Cem. Concr. Res. 136 (2020) 106194.
[13] B.L. Guo, Y.S. Tan, L. Wang, L. Chen, Z.L. Wu, K. Sasaki, V. Mechtcherine, D.C.W. Tsang, High-efficiency and low-carbon remediation of zinc contaminated sludge by magnesium oxysulfate cement, J. Hazard. Mater. 408 (2021) 124486.
[14] L. Wang, L. Chen, D.C.W. Tsang, Y.Y. Zhou, J. Rinklebe, H. Song, E.E. Kwon, K. Baek, Y.S. Ok, Mechanistic insights into red mud, blast furnace slag, or metakaolin-assisted stabilization/solidification of arsenic-contaminated sediment, Environ. Int. 133 (2019) 105247.
[15] M.B. Ogundiran, H.W. Nugteren, G.J. Witkamp, Immobilisation of lead smelting slag within spent aluminate–fly ash based geopolymers, J. Hazard. Mater. 248-249 (2013) 29–36.
[16] M.T. Zhang, C.H. Yang, M. Zhao, K. Yang, R. Shen, Y.J. Zheng, Immobilization potential of Cr(VI) in sodium hydroxide activated slag pastes, J. Hazard. Mater. 321 (2017) 281–289.
[17] Y.Q. Liu, W.P. Zhu, E.H. Yang, Alkali-activated ground granulated blast-furnace slag incorporating incinerator fly ash as a potential binder, Constr. Build. Mater. 112 (2016) 1005–1012.
[18] C.C. Fan, B.M. Wang, H.M. Ai, Y. Qi, Z. Liu, A comparative study on solidification/stabilization characteristics of coal fly ash-based geopolymer and Portland cement on heavy metals in MSWI fly ash, J. Clean. Prod. 319 (2021) 128790.
[19] W. Zhang, X.M. Liu, Z.Q. Zhang, Y.T. Li, J.R. Gu, Y.G. Wang, Y. Xue, Circulating fluidized bed fly ash-blast furnace slag based cementitious materials: hydration behaviors and performance, Constr. Build. Mater. 342 (2022) 128006.
[20] E. Kapeluszna, Ł. Kotwica, A. Różycka, Ł. Gołek, Incorporation of Al in C–A–S–H gels with various Ca/Si and Al/Si ratio: microstructural and structural characteristics with DTA/TG, XRD, FTIR and TEM analysis, Constr. Build. Mater. 155 (2017) 643–653.
[21] X.M. Liu, X.B. Zhao, H.F. Yin, J.L. Chen, N. Zhang, Intermediate-calcium based cementitious materials prepared by MSWI fly ash and other solid wastes: Hydration characteristics and heavy metals solidification behavior, J. Hazard. Mater. 349 (2018) 262–271.
[22] G.R. Qian, X.Y. Yang, S.X. Dong, J.Z. Zhou, Y. Sun, Y.F. Xu, Q. Liu, Stabilization of chromium-bearing electroplating sludge with MSWI fly ash-based Friedel matrices, J. Hazard. Mater. 165 (1-3) (2009) 955–960.
[23] R.P.W.J. Struis, M. Pasquali, L. Borgese, A. Gianoncelli, M. Gelfi, P. Colombi, D. Thiaudière, L.E. Depero, G. Rizzo, E. Bontempi, Inertisation of heavy metals in municipal solid waste incineration fly ash by means of colloidal silica—a synchrotron X-ray diffraction and absorption study, RSC Adv. 3 (34) (2013) 14339–14351.
[24] F.M. Yang, X. Zhou, F.J. Pang, W.J. Wang, W.L. Wang, Z.M. Wang, Heavy metal removal of solid waste source sulphoaluminate cement with graphene oxide, Constr. Build. Mater. 303 (2021) 124460.
[25] T. El-Hasan, M. Harfouche, A. Aldrabee, N. Abdelhadi, N. Abu-Jaber, G. Aquilanti, Synchrotron XANES and EXAFS evidences for Cr^{+6} and V^{+5} reduction within the oil shale ashes through mixing with natural additives and hydration process, Heliyon 7 (4) (2021) e06769.
[26] Y.C. Dai, G.R. Qian, Y.L. Cao, Y. Chi, Y.F. Xu, J.Z. Zhou, Q. Liu, Z.P. Xu, S.Z. Qiao, Effective removal and fixation of Cr(VI) from aqueous solution with Friedel's salt, J. Hazard. Mater. 170 (2-3) (2009) 1086–1092.
[27] J. Sun, L. Wang, J.J. Yu, B.L. Guo, L. Chen, Y.Y. Zhang, D.W. Wang, Z.X. Shen, D.C.W. Tsang, Cytotoxicity of stabilized/solidified municipal solid waste incineration fly ash, J. Hazard. Mater. 424 (2022) 127369.
[28] J. Li, S.Q. Zhang, Q. Wang, W. Ni, K.Q. Li, P.F. Fu, W.T. Hu, Z.F. Li, Feasibility of using fly ash–slag-based binder for mine backfilling and its associated leaching risks, J. Hazard. Mater. 400 (2020) 123191.
[29] S.Q. Zhang, T.Y. Shi, W. Ni, K.Q. Li, W. Gao, K. Wang, Y.Y. Zhang, The mechanism of hydrating and solidifying green mine fill materials using circulating fluidized bed fly ash-slag-based agent, J. Hazard. Mater. 415 (2021) 125625.
[30] C. Chen, G. Habert, Y. Bouzidi, A. Jullien, A. Ventura, LCA allocation procedure used as an incitative method for waste recycling: An application to mineral additions in concrete, Resour. Conserv. Recycl. 54 (12) (2010) 1231–1240.
[31] A. Paulu, M. Vitvarová, V. Kočí, Quantifying the industry-wide symbiotic potential: LCA of construction and energy waste management in the Czech Republic, Sustain. Prod. Consum. 34 (2022) 55–64.
[32] C. Li, S.P. Cui, Z.R. Nie, X.Z. Gong, Z.H. Wang, N. Itsubo, The LCA of Portland cement production in China, Int. J. Life Cycle Assess. 20 (1) (2015) 117–127.
[33] Y.Z. Cao, L.P. Guo, B. Chen, X.P. Fei, Modeling early age hydration kinetics and the hydrated phase of cement paste blended with chloride and sulfate, Constr. Build. Mater. 261 (2020) 120537.
[34] F. Pelisser, P.J.P. Gleize, A. Mikowski, Effect of the Ca/Si molar ratio on the micro/nanomechanical properties of synthetic C–S–H measured by nanoindentation, J. Phys. Chem. C 116 (32) (2012) 17219–17227.
[35] L. Black, A. Stumm, K. Garbev, P. Stemmermann, K.R. Hallam, G.C. Allen, X-ray photoelectron spectroscopy of the cement clinker phases tricalcium silicate and β-dicalcium silicate, Cem. Concr. Res. 33 (10) (2003) 1561–1565.
[36] X. Wang, W. Ni, J.J. Li, S.Q. Zhang, M. Hitch, R. Pascual, Carbonation of steel slag and gypsum for building materials and associated reaction mechanisms, Cem. Concr. Res. 125 (2019) 105893.
[37] B.G. Ma, X.H. Liu, H.B. Tan, T. Zhang, J.P. Mei, H.H. Qi, W.B. Jiang, F.B. Zou, Utilization of pretreated fly ash to enhance the chloride binding capacity of cement-based material, Constr. Build. Mater. 175 (2018) 726–734.
[38] J.W. Wang, Z.L. Hu, Y. Chen, J.L. Huang, Y.F. Ma, W.W. Zhu, J.P. Liu, Effect of Ca/Si and Al/Si on micromechanical properties of C(–A)–S–H, Cem. Concr. Res. 157 (2022) 106811.
[39] J.H. Huo, B.S. Yu, Z.G. Peng, Z.S. Wu, L.H. Zhang, Thermal control effects and mechanism of slag and fly ash on heat development of cement slurry used in hydrate formation, J. Nat. Gas Sci. Eng. 91 (2021) 103967.
[40] L. Liu, P. Yang, B. Zhang, C. Huan, L.J. Guo, Q.X. Yang, K.I. Song, Study on hydration reaction and structure evolution of cemented paste backfill in early-age based on resistivity and hydration heat, Constr. Build. Mater. 272 (2021) 121827.
[41] J.P. Dai, Q.C. Wang, X.Y. Lou, X.Y. Bao, B. Zhang, J.Q. Wang, X. Zhang, Solution calorimetry to assess effects of water-cement ratio and low temperature on hydration heat of cement, Constr. Build. Mater. 269 (2021) 121222.
[42] J.G. Hamilton, R.E. Farrell, N. Chen, R.F. Feng, J. Reid, D. Peak, Characterizing zinc speciation in soils from a smelter-affected boreal forest ecosystem, J. Environ. Qual. 45 (2) (2016) 684–692.

[43] Y.S. Feng, Y.J. Du, A.N. Zhou, M. Zhang, J.S. Li, S.J. Zhou, W.Y. Xia, Geoenvironmental properties of industrially contaminated site soil solidified/stabilized with a sustainable by-product-based binder, Sci. Total Environ. 765 (2021) 142778.
[44] Y.J. Du, M.L. Wei, K.R. Reddy, H.L. Wu, Effect of carbonation on leachability, strength and microstructural characteristics of KMP binder stabilized Zn and Pb contaminated soils, Chemosphere 144 (2016) 1033–1042.
[45] A. Manceau, L. Charlet, M.C. Boisset, B. Didier, L. Spadini, Sorption and speciation of heavy metals on hydrous Fe and Mn oxides. From microscopic to macroscopic, Appl. Clay Sci. 7 (1-3) (1992) 201–223.
[46] S. Bai, X.C. Guan, G.Y. Li, Early-age hydration heat evolution and kinetics of Portland cement containing nano-silica at different temperatures, Constr. Build. Mater. 334 (2022) 127363.
[47] Z.P. Li, D.G. Lu, X.J. Gao, Analysis of correlation between hydration heat release and compressive strength for blended cement pastes, Constr. Build. Mater. 260 (2020) 120436.
[48] Z.H. Xu, J.M. Gao, Y.S. Zhao, S.J. Li, Z.H. Guo, X. Luo, G.F. Chen, Promoting utilization rate of ground granulated blast furnace slag (GGBS): incorporation of nanosilica to improve the properties of blended cement containing high volume GGBS, J. Clean. Prod. 332 (2022) 130096.
[49] X.J. Lyu, G. Yao, Z.M. Wang, Q. Wang, L. Li, Hydration kinetics and properties of cement blended with mechanically activated gold mine tailings, Thermochim. Acta 683 (2020) 178457.
[50] E. Sobiecka, A. Obraniak, B. Antizar-Ladislao, Influence of mixture ratio and pH to solidification/stabilization process of hospital solid waste incineration ash in Portland cement, Chemosphere 111 (2014) 18–23.
[51] U.A. Birnin-Yauri, F.P. Glasser, Friedel's salt, $Ca_2Al(OH)_6(Cl,OH)\cdot 2H_2O$: Its solid solutions and their role in chloride binding, Cem. Concr. Res. 28 (12) (1998) 1713–1723.
[52] H.J. Li, H.H. Sun, X.C. Tie, X.J. Xiao, A new method to evaluate the hydraulic activity of Al–Si materials, Sci. China Ser. E Technol. Sci. 51 (2) (2008) 113–120.
[53] T.L. Barr, S. Seal, K. Wozniak, J. Klinowski, ESCA studies of the coordination state of aluminium in oxide environments, J. Chem. Soc. Faraday Trans. 93 (1) (1997) 181–186.
[54] P.K. Rasmussen, J.H. Sørensen, L.C. Hoang, B. Feddersen, F. Larsen, Notched connection in timber-concrete composite deck structures: a literature review on push-off experiments & design approaches, Constr. Build. Mater. 397 (2023) 131761.